
Article:
Lu, Jiadong, Zhang, Xiaokang, Hu, Yihua et al. (3 more authors) (2018) Independent Phase Current Reconstruction Strategy for IPMSM Sensorless Control Without Using Null Switching States. IEEE Transactions on Industrial Electronics. pp. 4492-4502. ISSN: 0278-0046

https://doi.org/10.1109/TIE.2017.2767542

Independent Phase Current Reconstruction Strategy for IPMSM Sensorless Control Without Using Null Switching States

Jiadong Lu, Xiaokang Zhang, Yihua Hu, *Senior Member, IEEE,* Jinglin Liu, *Member, IEEE,* Chun Gan, *Member, IEEE,* and Zheng Wang, *Senior Member, IEEE*

***Abstract*—This paper proposes a new phase current reconstruction scheme without using null switching states for IPMSM sensorless control. The phase currents are independently reconstructed and no additional test voltage pulses are required. Firstly, the principle of the basic phase current reconstruction for IPMSM drive system is analyzed in detail. Then, an independent phase current reconstruction scheme without using null switching states is proposed. The current reconstruction dead zone is divided into six sectors, and each sector is split into three parts with corresponding vector synthesis methods. Meanwhile, the null switching states, V_{000} and V_{111}, are removed from the proposed scheme. In this case, the zero vector is synthesized by the other available vectors. Finally, the reconstructed three-phase currents are utilized for high frequency (HF) sine-wave voltage injection based position estimation. The effectiveness of the proposed scheme is verified by experimental results on a 5kW IPMSM motor prototype, which shows that the reconstructed phase currents track the actual currents accurately in different working conditions.**

***Index Terms*—Fault tolerance, high frequency voltage injection, interior permanent magnet synchronous motor (IPMSM), phase current reconstruction, sensorless control.**

I. INTRODUCTION

THANKS to its outstanding features of high efficiency, high power density, and good dynamic properties, interior permanent magnet synchronous motors (IPMSMs) are now widely used in industry and daily life [1]-[3]. To achieve excellent performance for the whole system, many advanced control schemes have been proposed which commonly have a stringent demand for the accuracy of the rotor position and three-phase current values. Considering reliability and cost efficiency, indirect detection methods of the rotor position and three-phase currents, i.e., sensorless control [1]-[13] and phase current reconstruction technology [14]-[26], have been found to be alternatives for corresponding hardware components.

Over the decades, different phase current reconstruction schemes have been proposed. In [20], [21], [23], and [27] phase current reconstruction methods using space vector modulation are stated for three-phase PWM converter systems. Papers [23] and [28] describe the phase current reconstruction methods for DC-link currents in three-level converters. Paper [19] sets forward the control methods under the overmodulation mode with single DC-link current sensor. In [22] and [29], phase current reconstruction used in multi-phase systems is studied. The minimum injected voltages and sequence control to avoid abrupt changes in the amplitudes of the injected signals are raised for mid- and high-speed operation in [30]. Paper [31] aims to reveal an offset jitter-like waveform error, which is usually presented in all three-phase current signals reconstructed from DC-link current samples. Papers [25] and [32] focus on current reconstruction range extension. In [25] a hybrid PWM technique is proposed to reduce current distortions. However, two different PWM schemes are required to combine in the PWM generation strategy, which is complex.

Sensorless control technologies have been investigated over the decades, mainly including two typical methods which are the model based method and saliency-tracking based method [2], [4]-[7]. For the standstill and low-speed conditions, the saliency-tracking based methods have higher accuracy and better robustness, whereas the model based methods have higher error due to the lower signal to noise ratio (SNR) [7]. Considering the injected signal types, the high frequency (HF) injection methods can be classified into: the sine-wave voltage injection and square-wave voltage injection. The sine-wave voltage injection methods are simpler and easier for implementation, and thus this kind of methods are commonly used for sensorless control [4]-[6], [9]. This paper is to design the sensorless control scheme based on phase current

Manuscript received June 02, 2017; revised August 21, 2017 and September 28, 2017; accepted October 16, 2017. This work was supported by Shaanxi Science Technology Co-ordination and Innovation Project, China (2013KTCQ01-20, 2016KTCQ01-49). *(Corresponding author: Jinglin Liu).*

J. Lu, X. Zhang, and J. Liu are with the School of Automation, Northwestern Polytechnical University, and Shaanxi Key Laboratory of Small & Special Electrical Machine and Drive Technology, Xi'an 710129, China. (E-mail: noodle@mail.nwpu.edu.cn, dingdongdan@mail.nwpu.edu.cn, jinglinl@nwpu.edu.cn).

Y. Hu is with the Department of Electrical Engineering and Electronics, University of Liverpool, Liverpool L69 3GJ, U.K. (E-mail: y.hu35@liverpool.ac.uk).

C. Gan is with the Department of Electrical Engineering and Computer Science, University of Tennessee, Knoxville TN 37996, USA. (E-mail: cgan@utk.edu).

Z. Wang is with the School of Electrical Engineering, Southeast University, Nanjing 210096, China. (E-mail: zwang@eee.hku.hk).

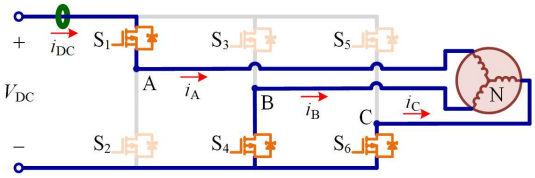

Fig. 1. Current flows of three phase inverter fed IPMSM drive system with switching state of V_{100}.

TABLE I
RELATIONSHIPS BETWEEN I_{DC} AND THREE PHASE CURRENTS UNDER DIFFERENT SWITCHING STATES.

Vector	V_{000}	V_{100}	V_{110}	V_{010}	V_{011}	V_{001}	V_{101}	V_{111}
i_{DC}	0	i_A	$-i_C$	i_B	$-i_A$	i_C	$-i_B$	0

reconstruction technique for IPMSM in low speed operations, and thus the HF sine-wave voltage injection strategy is employed in this paper.

The HF current response contains the information of the rotor position. Hence, accurate three-phase current values should be detected in order to obtain a precise rotor position. In common IPMSM drive systems, the motor three-phase currents are obtained by measuring two of the currents through current sensors, and calculating the third one indirectly from the two previously detected values. This method is adequate for the speed-control purpose, whereas for the aim of position estimation, this kind of method may face the problem of inaccuracy. The HF current responses are usually minuscule, which are prone to be affected by system white noise and other perturbations compared to the fundamental currents during current sampling process [4]. Besides, in the phase current reconstruction scheme (with one single current sensor) the two phase currents used to calculate the third one are not sampled at the same time, which brings additional errors to the third one. Therefore, independent detection of the three-phase currents is necessary for an accurate IPMSM sensorless control system using one single current sensor.

In this paper, an IPMSM sensorless control strategy with independent phase current reconstruction is proposed and studied, where the null switching state vectors, i.e., V_{000} and V_{111}, are not utilized. Under this circumstance, an equivalent zero vector is synthesized by the rest six available vectors. To make independent three-phase current detection possible, in the proposed scheme, the current reconstruction dead zone is divided into six sectors, and each sector is split into three parts using different vector synthesis methods. Because the current reconstruction sampling points are within the period of the action vectors, no additional voltage pulse is needed for current reconstruction. The reconstructed three-phase currents are afterward applied for position estimation. By utilizing the independent phase current reconstruction strategy, the reconstructed three-phase currents track the actual currents precisely, which is essential for position estimation in an IPMSM sensorless control system.

This paper is organized as follows. In Section II, the basic principle of phase current reconstruction method is illustrated. In Section III, an independent phase current reconstruction scheme is proposed accordingly. In Section IV, HF voltage injection sensorless control scheme using one single current sensor is described. In Section V, experimental results are presented. The conclusion is given finally.

II. PRINCIPLE OF BASIC PHASE CURRENT RECONSTRUCTION

A DC-link current sensor can theoretically be used for both DC-bus current detection (overcurrent protection) and phase current reconstruction. As shown in Fig.1, the DC current value i_{DC} is the same as the value of phase-A current i_A under the switching state of V_{100}. It is worth noting that the currents in Fig.1 are in the defined positive direction.

Obviously, in Fig.1 the inverter has six active switching state vectors, namely, V_{100} (V_1), V_{110} (V_2), V_{010} (V_3), V_{011} (V_4), V_{001} (V_5), V_{101} (V_6), and two null switching state vectors V_{000} and V_{111}. Table I shows the relationships among i_{DC} and three-phase currents in eight switching states respectively. From Table I, it states apparently that i_A can be detected from i_{DC} with switching states V_{100} and V_{011} (defined as group 1), i_B with V_{010} or V_{101} (defined as group 2), and i_C with V_{001} or V_{110} (defined as group 3). Among the eight vectors the two zero vectors V_{000} and V_{111} cannot be applied for phase current reconstruction because i_{DC} is zero in null switching states. To obtain the values of three-phase currents, vectors from at least two groups are required. Taking the independent phase current reconstruction scheme into account, vectors from all the three groups are needed.

However, due to the switching device dead time, diode recovery time, and AD sampling time, the minimum duration T_{min} for each active vector within one PWM cycle time T_s is needed to realize precise sampling for current reconstruction [24]. In some regions, the duration of active voltage vectors may be shorter than T_{min}, which is not possible to reconstruct the current. These regions lead to current reconstruction dead zones, as shown in Fig.2 (a). The output voltage area consists of the normal areas and the current reconstruction dead zones, and these dead zones are composed of the sector boundary areas and low modulation areas.

III. INDEPENDENT PHASE CURRENT RECONSTRUCTION SCHEME USING ONE SINGLE DC CURRENT SENSOR

A. Division of Reconstruction Dead Zones and Voltage Synthesis Scheme

In Fig.2 (b) the current reconstruction dead zone is divided into six sectors. In this paper, sector I is applied for illustration, and the situations in the rest five sectors are similar. Concerning circular output voltage applications, the parts of dead zone within the circular output voltage are discussed in this paper. To implement the independent phase current reconstruction scheme, in Fig.3 sector I is split into three parts and in each part the vectors applied are from all the three groups. To be specific, in part 1, V_4 (group 1), V_6 (group 2), and V_2 (group 3) are utilized for vector synthesis and current reconstruction. In part 2, V_1, V_4 (group 1), V_6 (group 2), and V_2 (group 3) are applied. While in part 3, V_1 (group 1), V_6 (group 2), and V_2 (group 3) are used. It is worth noting that in each part, the action time of each basic vector is longer than T_{min}. The basic vectors used in the

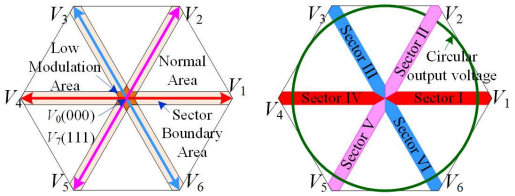

Fig. 2. Current reconstruction dead zones and defined six dead zone sectors.

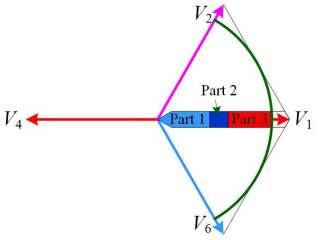

Fig. 3. Sector I of reconstruction dead zones and defined three parts.

TABLE II
BASIC VECTORS USED IN THE THREE DEFINED PARTS FOR EACH SECTOR.

Sector	Part	Group 1	Group 2	Group 3
I	1	V_4	V_6	V_2
	2	V_1, V_4	V_6	V_2
	3	V_1	V_6	V_2
II	1	V_1	V_3	V_5
	2	V_1	V_3	V_2, V_5
	3	V_1	V_3	V_2
III	1	V_4	V_6	V_2
	2	V_4	V_3, V_6	V_2
	3	V_4	V_3	V_2
IV	1	V_1	V_3	V_5
	2	V_1, V_4	V_3	V_5
	3	V_4	V_3	V_5
V	1	V_4	V_6	V_2
	2	V_4	V_6	V_2, V_5
	3	V_4	V_6	V_5
VI	1	V_1	V_6	V_5
	2	V_1	V_3, V_6	V_5
	3	V_1	V_6	V_5

three defined parts for each sector is displayed in Table II. Additionally, the largest area of the output voltage in sector I using the basic vectors in Table II is shown in Fig.4. In Fig.4, T_{V1}, T_{V2}, T_{V4}, and T_{V6} represent action time of vectors V_1, V_2, V_4, and V_6 within one PWM cycle period, respectively. T_{V1}, ∇T_{V2}, ∇T_{V4}, and ∇T_{V6} are the gradient directions of T_{V1}, T_{V2}, T_{V4}, and T_{V6} respectively, which denote the increasing direction of T_{V1}, T_{V2}, T_{V4}, and T_{V6}.

In Fig.4 (a), the area within the green triangle represents the output voltage vector range synthesized by the three basic vectors V_2, V_4, and V_6. The three boundary lines marked with ①, ②, and ③ represent the conditions when T_{V4}, T_{V6}, and T_{V2} reach the lower limit of T_{min}, respectively. The three vertices of the triangle represent the conditions that T_{V2}, T_{V4}, and T_{V6} reach the upper limit of T_s-2T_{min}, which means that the other two corresponding action time periods reach the lower limit of T_{min}. The value of $|Oa|$ in Fig.4 (a) is

$$|Oa| = T_s/2 - 3T_{min}/2 . \quad (1)$$

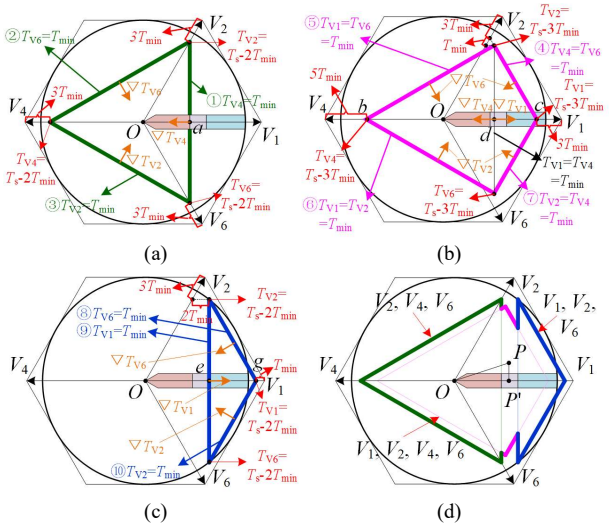

Fig. 4. Maximum output voltage area: (a) V_2, V_4, and V_6, (b) V_1, V_2, V_4, and V_6, (c) V_1, V_2, and V_6, (d) United area of the output voltage.

In Fig.4 (b), the area within the pink quadrilateral represents the output voltage vector range synthesized by the four basic vectors of V_1, V_2, V_4, and V_6. The four boundary lines marked with ④, ⑤, ⑥, and ⑦ represent the conditions when two of T_{V1}, T_{V2}, T_{V4}, and T_{V6} reached the lower limit of T_{min}, which is illustrated in Fig.4 (b) in detail. The four vertices of the quadrilateral represent the situations that T_{V1}, T_{V2}, T_{V4}, and T_{V6} reach the upper limit of T_s-3T_{min}, which means that the other three corresponding action periods reach the lower limit of T_{min}. The values of $|Ob|$, $|Oc|$, $|Od|$ in Fig.4 (b) are

$$\begin{cases} |Ob| = T_s - 5T_{min} \\ |Oc| = T_s - 3T_{min} \\ |Od| = T_s/2 - T_{min} \end{cases} . \quad (2)$$

In Fig.4 (c), the area within the blue triangle represents the output voltage vector range synthesized by the three basic vectors of V_1, V_2, and V_6. The three boundary lines marked with ⑧, ⑨, and ⑩ represent the conditions when T_{V6}, T_{V1}, and T_{V2} reach the lower limit of T_{min}. The three vertices of the triangle represent the cases that T_{V1}, T_{V2}, and T_{V6} reach the upper limit of T_s-2T_{min}, which means that the other two corresponding action time periods reach the lower limit of T_{min}. The values of $|Oe|$ and $|Og|$ in Fig.4 (c) are

$$\begin{cases} |Oe| = T_s/2 + T_{min}/2 \\ |Og| = T_s - T_{min} \end{cases} . \quad (3)$$

Fig.4 (d) shows the united output voltage vector scope by applying the proposed synthesis method. When the output vector falls in part 1 of sector I, the basic vectors V_2, V_4 and V_6 are used for vector synthesis, whereas V_1, V_2, V_4, and V_6 are used in part 2, and V_1, V_2, and V_6 are used in part 3.

B. Independent Phase Current Reconstruction Scheme

From Fig.4 (d) it is apparent that the united output voltage

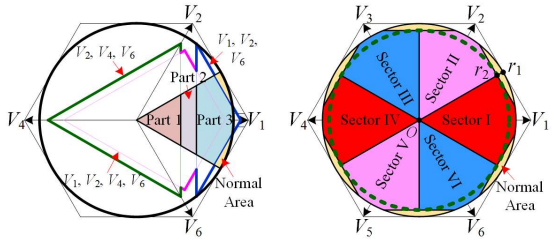

Fig. 5. Independent phase current reconstruction scheme: (a) Expanded defined three parts in sector I; (b) Expanded six current reconstruction sectors.

area of the proposed synthesis method is much larger than the current reconstruction dead zone in sector I. In addition, the area of the output voltage covers most of the normal area between the lower border of sector II and the upper border of VI. Therefore, in order to apply the independent phase current reconstruction scheme, in the normal areas where the united area of the output voltage area is covered, the proposed vector synthesis methods should be utilized. Hence, the defined three parts in Fig.3 can be expanded as shown in Fig.5 (a), and the corresponding expanded six independent current reconstruction sectors are illustrated in Fig.5 (b).

In Fig.5 (b), the defined six current reconstruction sectors cover most of the circular area of the voltage output, where only six small normal areas are not included. $|Or_1|$ and $|Or_2|$ represent the circular voltage output area of the normal and proposed voltage synthesis strategy respectively

$$\begin{cases} |Or_1| = T_s \cdot \sqrt{3}/2 \\ |Or_2| = |Og| \cdot \sqrt{3}/2 = (T_s - T_{\min}) \cdot \sqrt{3}/2 \end{cases}. \tag{4}$$

Compared to the normal circular area, the voltage output range is reduced by

$$\left(|Or_1| - |Or_2|\right)/|Or_1| = T_{\min}/T_s \ . \tag{5}$$

Because $T_{\min}$ is very small compared to T_s, compared to the normal circular area, the voltage range reduction of the proposed strategy is negligible. The output voltage range is almost the same as that of the normal one. The aim of this paper is to study the independent phase current reconstruction strategy used in sensorless control. Therefore, the actual area of the output voltage vector in this paper is limited in the green dashed circle, as shown in Fig.5 (b).

C. Action Time of Basic Vectors

In this paper, sector I is taken as an example to calculate the action time of the basic vectors. In Fig.4 and Fig.5 (a) the same scale is used. In this section, the distance between each pair of points used is illustrated in Fig.4. In the previous part, each current reconstruction dead zone is divided into three parts with different vector synthesis methods, i.e., parts 1, 2, and 3 as shown in Fig.5 (a). The action time of the three parts is studied in turns. Assuming a terminal point $P(x, y)$ (per-unit value, in the two-phase static coordinate system) of the output voltage vector falls in sector I as shown in Fig.4 (d), the distance of $|OP'|$ is x and the distance of $|PP'|$ is y.

1) Part 1

In part 1, V_2, V_4, and V_6 are utilized. In Fig.4 (d), if $|OP'|$ is shorter than $|Oa|/T_s$, as shown in (6), the vector falls in part 1

$$x \le |Oa|/T_s = 1/2 - 3T_{\min}/2T_s \ . \tag{6}$$

The action time of V_2, V_4, and V_6 can be calculated as

$$T_{V2} = T_{\min} + \frac{2|Oa| + x \cdot T_s}{3} + \frac{y \cdot T_s}{\sqrt{3}} = \frac{1 + x + \sqrt{3}y}{3} \cdot T_s \tag{7}$$

$$T_{V4} = T_{\min} + 2\left(|Oa| - x \cdot T_s\right)/3 = (1 - 2x)T_s/3 \tag{8}$$

$$T_{V6} = T_{\min} + \frac{2 \cdot |Oa| + x \cdot T_s}{3} - \frac{y \cdot T_s}{\sqrt{3}} = \frac{1 + x - \sqrt{3}y}{3} \cdot T_s \tag{9}$$

in this paper T_{V1}, T_{V2}, T_{V3}, T_{V4}, T_{V5}, and T_{V6} represent the action time of vectors V_1, V_2, V_3, V_4, V_5, and V_6 within one PWM cycle period, respectively.

2) Part 2

In part 2, V_1, V_2, V_4, and V_6 are utilized. If $|OP'|$ is longer than $|Oa|/T_s$ and shorter than $|Od|/T_s$, the vector falls in part 2

$$\begin{cases} x > |Oa|/T_s = 1/2 - 3T_{\min}/2T_s \\ x \le |Oe|/T_s = 1/2 + T_{\min}/2T_s \end{cases}. \tag{10}$$

The action time of the four vectors V_1, V_2, V_4, and V_6 is:

In case of $x \le |Od|/T_s$

$$T_{V1} = T_{\min} \tag{11}$$

$$\begin{aligned} T_{V2} &= T_{\min} + \left(|Ob| + x \cdot T_s\right)/3 + \left(y \cdot T_s\right)/\sqrt{3} \\ &= \left(1 - 2T_{\min}/T_s + x + \sqrt{3}y\right)T_s/3 \end{aligned} \tag{12}$$

$$T_{V4} = T_{\min} + 2 \cdot \left(|Od| - x \cdot T_s\right)/3 = \left(1 + T_{\min}/T_s - 2x\right) \cdot T_s/3 \tag{13}$$

$$\begin{aligned} T_{V6} &= T_{\min} + \left(|Ob| + x \cdot T_s\right)/3 - y \cdot T_s/\sqrt{3} \\ &= \left(1 - 2T_{\min}/T_s + x - \sqrt{3}y\right)T_s/3 \end{aligned} \tag{14}$$

In case of $x > |Od|/T_s$

$$T_{V1} = T_{\min} + 2 \cdot \left(x \cdot T_s - |Od|\right) = \left(-1 + 3T_{\min}/T_s + 2x\right) \cdot T_s \tag{15}$$

$$\begin{aligned} T_{V2} &= T_{\min} + \left(|Oc| - x \cdot T_s\right) + y \cdot T_s/\sqrt{3} \\ &= \left(1 - 2T_{\min}/T_s - x + y/\sqrt{3}\right) \cdot T_s \end{aligned} \tag{16}$$

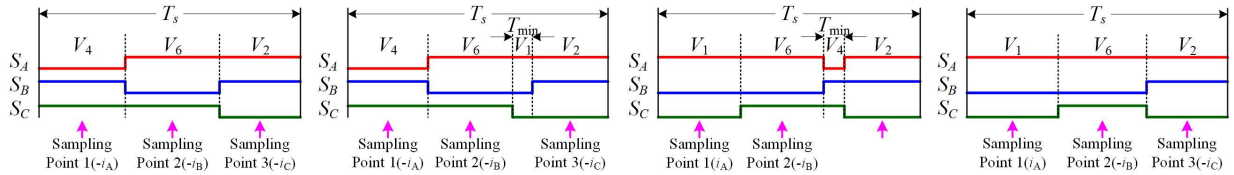

Fig. 6. PWM synthesis strategy and current sampling points in defined sector I: (a) Part 1, (b) Part 2 ($x \le |Od|/T_s$), (c) Part 2 ($x > |Od|/T_s$), (d) Part 3.

TABLE III
VARIABLES TO REPLACE x AND y IN EQUATIONS (6)-(22)

Sector	Variable to replace x	Variable to replace y
I	x	y
II	$x/2+\sqrt{3}\,y/2$	$-\sqrt{3}\,x/2+y/2$
III	$-x/2+\sqrt{3}\,y/2$	$-\sqrt{3}\,x/2-y/2$
IV	$-x$	$-y$
V	$-x/2-\sqrt{3}\,y/2$	$\sqrt{3}\,x/2-y/2$
VI	$x/2-\sqrt{3}\,y/2$	$\sqrt{3}\,x/2+y/2$

TABLE IV
VARIABLES TO REPLACE T_{V1}, T_{V1}, T_{V1}, AND T_{V6} IN EQUATIONS (6)-(22)

Sector	V_1, T_{V1}	V_2, T_{V2}	V_4, T_{V4}	V_6, T_{V6}
I	V_1, T_{V1}	V_2, T_{V2}	V_4, T_{V4}	V_6, T_{V6}
II	V_2, T_{V2}	V_3, T_{V3}	V_5, T_{V5}	V_1, T_{V1}
III	V_3, T_{V3}	V_4, T_{V4}	V_6, T_{V6}	V_2, T_{V2}
IV	V_4, T_{V4}	V_5, T_{V5}	V_1, T_{V1}	V_3, T_{V3}
V	V_5, T_{V5}	V_6, T_{V6}	V_2, T_{V2}	V_4, T_{V4}
VI	V_6, T_{V6}	V_1, T_{V1}	V_3, T_{V3}	V_5, T_{V5}

$$T_{V4} = T_{\min} \tag{17}$$

$$\begin{aligned} T_{V6} &= T_{\min} + \left(|Oc| - x\cdot T_s\right) - y\cdot T_s/\sqrt{3} \\ &= \left(1 - 2T_{\min}/T_s - x - y/\sqrt{3}\right)\cdot T_s \end{aligned} . \tag{18}$$

3) Part 3

In part 3, V_1, V_2, and V_6 are utilized. If $|OP'|$ is longer than $|Oe|/T_s$, the vector falls in part 3

$$x > |Oe|/T_s = 1/2 + T_{\min}/2T_s . \tag{19}$$

Action time of the three vectors V_1, V_2, and V_6 are

$$T_{V1} = T_{\min} + 2\left(x\cdot T_s - |Oe|\right) = \left(-1 + 2x\right)\cdot T_s \tag{20}$$

$$T_{V2} = T_{\min} + \left(|Og| - x\cdot T_s\right) + y\cdot T_s/\sqrt{3} = \left(1 - x + y/\sqrt{3}\right)\cdot T_s \tag{21}$$

$$T_{V6} = T_{\min} + \left(|Og| - x\cdot T_s\right) - y\cdot T_s/\sqrt{3} = \left(1 - x - y/\sqrt{3}\right)\cdot T_s . \tag{22}$$

It should be noted that in different sectors the methods are similar, whereas variables x and y in (6)-(22) should be replaced by $|OP'|$ and $|PP'|$ as shown in Table III. In this table P' is the projection point on the corresponding vector. Besides, T_{V1}, T_{V2}, T_{V4}, T_{V6} should be replaced by the variables in Table IV.

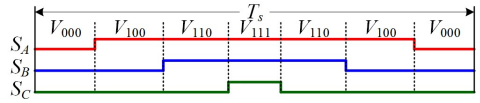

Fig. 7. Diagram of the seven-segment PWM waveform in the conventional SVPWM algorithm.

D. PWM Synthesis Method and Current Sampling Points

To implement the proposed current reconstruction strategy, the PWM synthesis method and current sampling points for the DC current is presented in Fig.6, where the PWM synthesis method in the defined three parts of current reconstruction in sector I is illustrated.

Fig.7 shows the seven-segment PWM waveform by using the conventional SVPWM algorithm [24]. This type of PWM waveform is widely used in the IPMSM control systems, and there are six commutation points for the switching devices during each PWM cycle. In Fig.6 (a), (b), and (c), there are also six commutation points in each PWM cycle, whereas four in Fig.6 (d). Compared to the seven-segment PWM waveform, the switching times are not increased by employing the proposed strategy. Compared to the current reconstruction strategy utilizing additional testing voltage pulses [17], the switching times of the proposed method are reduced as well. Therefore, the switching losses of the proposed strategy are the same as those in the conventional seven-segment PWM strategies.

IV. SENSORLESS CONTROL SCHEME

The sine-wave HF voltage injection strategy is applied in this paper to estimate the rotor position. The HF voltage signals are generated by the proposed vector synthesis method, and the HF current responses are reconstructed from the DC-bus current by the proposed independent phase current reconstruction scheme. The injected signal is given below

$$u_h = u_{\alpha h} + i u_{\beta h} = U_h e^{i\omega_h t} \tag{23}$$

in which u_h is the injected HF voltage; $u_{\alpha h}$ and $u_{\beta h}$ are the HF voltages in the Clark reference frame; U_h and ω_h represent the HF voltage amplitude and angular velocity respectively.

The mathematical model of the IPMSM is given by [5]

$$\begin{aligned} \begin{bmatrix} u_\alpha \\ u_\beta \end{bmatrix} &= R\cdot\begin{bmatrix} i_\alpha \\ i_\beta \end{bmatrix} + \begin{bmatrix} L_0 + L_2\cos 2\theta & L_2\sin 2\theta \\ L_2\sin 2\theta & L_0 - L_2\cos 2\theta \end{bmatrix} \times \frac{\mathrm{d}}{\mathrm{d}t}\begin{bmatrix} i_\alpha \\ i_\beta \end{bmatrix} \\ &+ \frac{\mathrm{d}\theta}{\mathrm{d}t}\left(2L_2\begin{bmatrix} -\sin 2\theta & \cos 2\theta \\ \cos 2\theta & \sin 2\theta \end{bmatrix}\begin{bmatrix} i_\alpha \\ i_\beta \end{bmatrix} + \psi_f \begin{bmatrix} -\sin\theta \\ \cos\theta \end{bmatrix}\right) \end{aligned} \tag{24}$$

$$\begin{cases} L_0 = \left(L_\mathrm{d} + L_\mathrm{q}\right)/2 > 0 \\ L_2 = \left(L_\mathrm{d} - L_\mathrm{q}\right)/2 < 0 \end{cases} \tag{25}$$

where u_α, u_β and i_α, i_β are the motor voltages and currents in the Clark reference frame, respectively; R is the motor resistance; L_d and L_q are the d- and q-axis stator inductances; θ is the actual rotor position; ψ_f is flux linkage of the permanent magnet.

By neglecting the first and third items in (24), the mathematical model of the IPMSM is given by

$$\begin{bmatrix} u_{\alpha\mathrm{h}} \\ u_{\beta\mathrm{h}} \end{bmatrix} = \begin{bmatrix} L_0 + L_2\cos(2\theta) & L_2\sin(2\theta) \\ L_2\sin(2\theta) & L_0 - L_2\cos(2\theta) \end{bmatrix} \cdot \frac{\mathrm{d}}{\mathrm{d}t} \begin{bmatrix} i_{\alpha\mathrm{h}} \\ i_{\beta\mathrm{h}} \end{bmatrix} \tag{26}$$

where $i_{\alpha\mathrm{h}}$ and $i_{\beta\mathrm{h}}$ are the HF currents in Clark reference frame.

The HF current response can be calculated from (23)-(26)

$$\begin{bmatrix} i_{\mathrm{Ah}} \\ i_{\mathrm{Bh}} \\ i_{\mathrm{Ch}} \end{bmatrix} = k\left\{ L_0 \cdot \begin{bmatrix} \sin(\omega_\mathrm{h} t) \\ \sin(\omega_\mathrm{h} t - 2\pi/3) \\ \sin(\omega_\mathrm{h} t + 2\pi/3) \end{bmatrix} - L_2 \cdot \begin{bmatrix} \sin(\omega_\mathrm{h} t - 2\theta) \\ \sin(\omega_\mathrm{h} t - 2\theta + 2\pi/3) \\ \sin(\omega_\mathrm{h} t - 2\theta - 2\pi/3) \end{bmatrix} \right\} \tag{27}$$

$$k = U_\mathrm{h} / \left(\omega_\mathrm{h} L_\mathrm{d} L_\mathrm{q}\right) > 0 \tag{28}$$

where i_{Ah}, i_{Bh}, and i_{Ch} represent the three-phase HF currents.

Thus, the positive and negative sequences of HF current in phase A can be deduced from (27) and (28)

$$\begin{cases} i_{\mathrm{Ah\_P}} = kL_0 \sin(\omega_\mathrm{h} t) \\ i_{\mathrm{Ah\_N}} = -kL_2 \sin(\omega_\mathrm{h} t - 2\theta) \end{cases} \tag{29}$$

where $i_{\mathrm{Ah\_P}}$ and $i_{\mathrm{Ah\_N}}$ are the positive and negative sequences of HF current in phase A.

In (29) the phase angle of each component of phase A can be utilized for position estimation which is given by

$$\begin{cases} \phi_{\mathrm{Ah\_P}} = \omega_\mathrm{h} t \\ \phi_{\mathrm{Ah\_N}} = \omega_\mathrm{h} t - 2\theta \end{cases} \tag{30}$$

$$\theta = \left(\phi_{\mathrm{Ah\_P}} - \phi_{\mathrm{Ah\_N}}\right)/2 \tag{31}$$

where $\phi_{\mathrm{Ah\_P}}$, $\phi_{\mathrm{Ah\_N}}$ are respectively the phase of $i_{\mathrm{Ah\_P}}$ and $i_{\mathrm{Ah\_N}}$.

In this paper, the least squares fitting algorithm is utilized to extract the phase angle of HF current responses. A HF current response signal can be expressed as

$$\begin{aligned} y[n] &= \mathrm{AMP} \cdot \cos\left(2\pi n \cdot \omega_\mathrm{h}/\omega_\mathrm{s} + \varphi\right) \\ &= \mathrm{AMP} \cdot \cos\varphi \cdot \cos\left(2\pi n \cdot \omega_\mathrm{h}/\omega_\mathrm{s}\right) - \\ &\quad \mathrm{AMP} \cdot \sin\varphi \cdot \sin\left(2\pi n \cdot \omega_\mathrm{h}/\omega_\mathrm{s}\right) \end{aligned} \tag{32}$$

where $y[n]$ (n=1, 2, ...) is the sampling values of the HF current; AMP represents the amplitude of the signal; ω_s denotes the signal sampling angular velocity; φ is the angle to be extracted.

For each value of n, $\cos[2\pi\cdot(\omega_h/\omega_s)\cdot n]$ and $\sin[2\pi\cdot(\omega_h/\omega_s)\cdot n]$ are constant values in (32), which are defined as $Q_1[n]$ and $Q_2[n]$ respectively. By defining α_1=AMP·cos(φ) and α_2= AMP·sin(φ) for variable replacement, (32) can be further expressed as

$$y[n] = Q_1[n]\cdot\alpha_1 - Q_2[n]\cdot\alpha_2 \tag{33}$$

The coefficients α_1 and α_2 can be obtained by applying least squares fitting algorithm in (33), and the angle φ of the signal can be finally extracted.

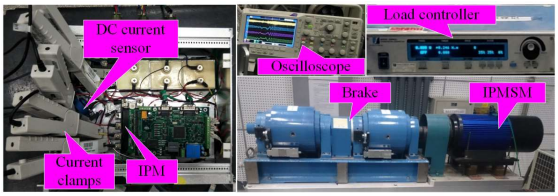

Fig. 8. Experimental setup.

TABLE V
MAIN PARAMETERS OF IPMSM FOR EXPERIMENT.

Parameter	Value	Parameter	Value
Rated power	5 kW	Pole pairs	3
Inverter DC voltage	540 V	*d*-axis Inductance	4.2 mH
Rated voltage	380 V	*q*-axis Inductance	10.1 mH
Rated current	8.5 A	Phase resistance	0.18 Ω
Efficiency	0.9	Maximum speed	3000 r/min
Rated torque	15 N·m		

V. EXPERIMENTAL RESULTS

In order to validate the correctness of the proposed independent phase current reconstruction scheme, an experiment platform is set up which is shown in Fig.8. The main parameters of IPMSM motor prototype are given in Table V. The controller is supplied by a three-phase AC voltage of 380 V, with a rectifier and a multi-level DC output power converter installed. The MAGTROL 30 kW dynamometer with torque sensors installed is utilized to test the load performances of the system. An intelligent power module (IPM), Mitsubishi PM75RLA120, is used as the PWM-VSI with the frequency of 8 kHz. The DC-bus current, which is used to reconstruct the three-phase currents, is sampled by an isolated hall-effect current sensor (HS01-100, maximum sample rate 100 kHz). The four white current clamps are used to sample the DC-bus and three-phase currents for comparison. On the platform, a DSP, TMS320F2812, is utilized to implement the proposed strategy, sample DC currents, and generate PWM signals, etc. In the experiment setup, the minimum switching time $T_{\min}$ is 10 μs. In this paper, all the reconstructed phase currents are calculated in DSP using the DC-bus current. Then the reconstructed phase currents are transmitted in real time through RS-485 to the host computer. For the comparison, the actual currents are obtained by additional phase current sensors and transmitted synchronously to the host computer.

The experimental results of the proposed independent phase current reconstruction strategy (here, Sector III, Part I) are

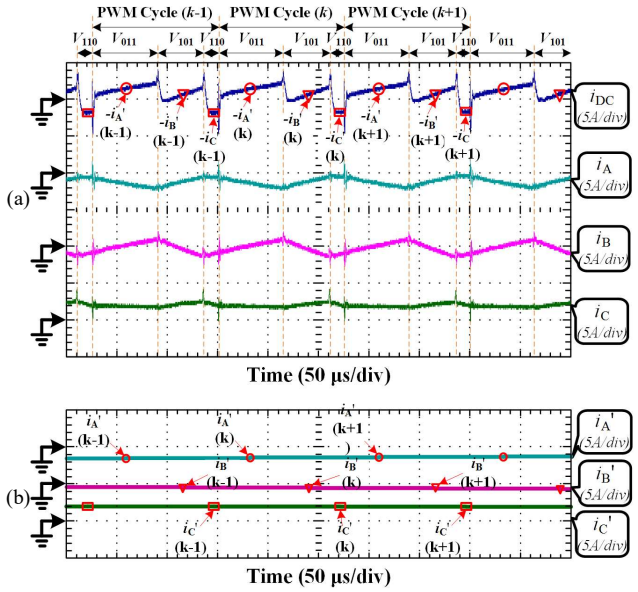

Fig. 9. Experimental results of proposed independent phase current reconstruction strategy (here, Sector III, Part 1): (a) DC-bus current and actual three phase currents, (b) Reconstructed three phase currents.

presented in Fig.9. In the figure, i_{DC} is the detected DC-bus current; i_A, i_B, and i_C represent actual three-phase currents respectively; i_A', i_B', and i_C' denote the reconstructed three-phase currents respectively; (k-1), (k), and (k+1) represent the PWM cycle sequence. The reconstructed phase currents are calculated discretely with the PWM signals. In the experiments, the switching frequency is set to 8 kHz; therefore, the update frequency of the reconstructed current is also 8 kHz, which is updated every 125μs, as shown in Fig.9 (b). Each PWM cycle is 125 μs, where the three sampling points are in the middle of the corresponding vector periods, which are marked with different symbols. From Fig.9, it can be seen that the three-phase currents are independently reconstructed from the DC-bus current. The first sampling point with circular symbol in each PWM cycle derives the current i_A'; the second sampling point with inverted triangle symbol obtains the current i_B'; the third sampling point with square symbol extracts the current i_C'.

Fig.10 shows the experimental results of the actual and reconstructed three-phase currents together with the total harmonic distortion (THD) using the proposed current reconstruction strategy. It can be seen that the reconstructed three-phase currents track the actual ones accurately within an acceptable error. Compared with the errors in [15] and [24], there are no low-frequency components in the reconstruction errors. This is because the three-phase currents are independently reconstructed and no zero voltage vector sampling method (ZVVSM) is utilized. The high-frequency components in the reconstruction errors are mainly caused by current chopping effects and the differences between different current sensors for comparison and the corresponding signal conditioning circuits. Electromagnetic interference and white noise of the system are also the causes of the errors. Besides, by applying the independent phase current reconstruction strategy, the errors in the reconstructed three-phase currents are controlled within an acceptable range. The actual and

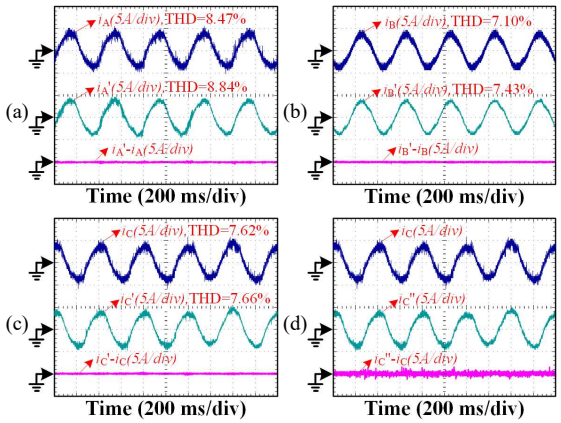

Fig. 10. Experimental results of actual and reconstructed currents and THD of: (a) Phase A, (b) Phase B, (c) Phase C, (d) Non-independent detection of phase C.

reconstructed phase current THD are also given in Fig.10. Compared to the conventional seven-segment SVPWM algorithm, the THD of the proposed PWM generating method is slightly larger. Whereas compared with other PWM synthesis strategies for current reconstruction in [15], [32], the THD of the proposed scheme are reduced.

In Fig.10 (d), the experimental results of non-independent reconstruction of phase current i_C" are illustrated. The non-independent reconstructed phase current i_C" is calculated according to the reconstructed phase currents i_A' and i_B'. From Fig.10 (c) and (d), it can be seen that, compared with the independent reconstructed phase current i_C', the non-independent reconstructed phase current i_C" has lager estimation error, which is approximately twice as the error of i_C'. This is caused by different sampling points of i_A' and i_B'. In Fig.6, i_A' and i_B' are reconstructed from sampling points 1 and 2 respectively in each PWM cycle. Therefore, taking the current chopping effect into account, in sampling point 2, the actual value of phase current in ideal conditions is

$$i_{A\_Sampling2} = i_A' + \Delta i_A' \tag{34}$$

where Δi_A' denotes the current increment of i_A' from sampling point 1 to 2 caused by current chopping effect.

As a result, under ideal conditions, at sampling point 2, the non-independent reconstructed phase current i_C" has an indefinite error Δi_A' compared to the actual current $i_{C\_Sampling2}$

$$\begin{cases} i_{C\_Sampling2} = -\left(i_{A\_Sampling2} + i_B'\right) \\ i_C'' = -\left(i_A' + i_B'\right) \end{cases} \tag{35}$$

$$\Delta i_C' = i_C'' - i_{C\_Sampling2} = \Delta i_A' \tag{36}$$

where $i_{C\_Sampling2}$ is the actual value of phase current i_C at sampling point 2; Δi_C' denotes the additional error of the non-independent reconstructed phase current i_C".

It should be noted that the error of the non-independent

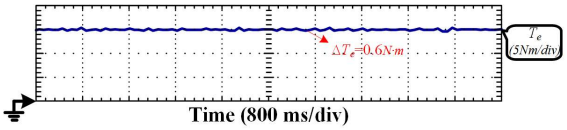

Fig. 11. Experimental results of the torque ripple in motor shaft end (500 rpm, 15 N·m).

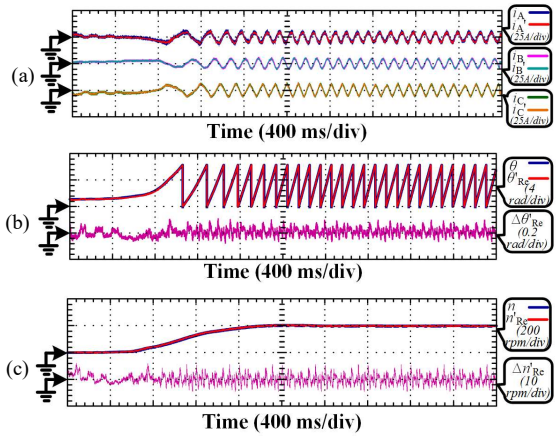

Fig. 12. Experimental results of actual and reconstructed three phase currents and position estimation in starting process: (a) Current reconstruction results, (b) Position estimation results, (c) Rotor speed.

reconstructed phase current i_C" also have other factors as those introduced by the independent reconstructed phase currents.

Fig.11 shows the experimental results of the torque ripple in the motor shaft end at 500 rpm with a rated load of 15 N·m. The torque curve is measured by the torque sensors inside the MAGTROL dynamometer. From the figure, it can be seen that the torque ripple by applying the proposed PWM synthesis method is about 0.6 N·m.

Fig.12 (a) shows the experimental results of the actual and reconstructed three-phase currents during starting. The reconstructed three-phase currents track the actual ones accurately even in the dynamic process with rapid current fluctuations. The actual and estimated rotor positions using reconstructed phase currents are presented in Fig. 12(b). In the figure θ and θ'_{Re} are the actual and estimated rotor positions using the reconstructed phase currents respectively; $\Delta\theta'_{\mathrm{Re}}$ denotes the estimation error of θ'_{Re}. From the figure, it can be observed that, the estimated rotor position tracks the actual one with a small error, which is controlled within ±0.2 rad (all angles are electrical angles). The rotor speed performance is shown in Fig. 12(c). The speed is obtained by simple low-pass filtering of differential operation of the estimated rotor position, which is shown in (37). In the figure, n and n'_{Re} are the actual and estimated rotor positions using the reconstructed phase currents respectively; $\Delta n'_{\mathrm{Re}}$ denotes the errors of n'_{Re}. The estimated rotor speed follows the actual one accurately, and the error can be controlled within 10 rpm.

$$n(k) = K \cdot n(k-1) + (1-K) \cdot (30\Delta\theta) / (\pi p \cdot \Delta t) \quad (37)$$

where $n(k)$ is the discrete output speed value; $\Delta\theta$ is the discrete rotor position increment; K denotes the coefficient of the filter; Δt represents discrete time interval; p is the rotor pole pairs.

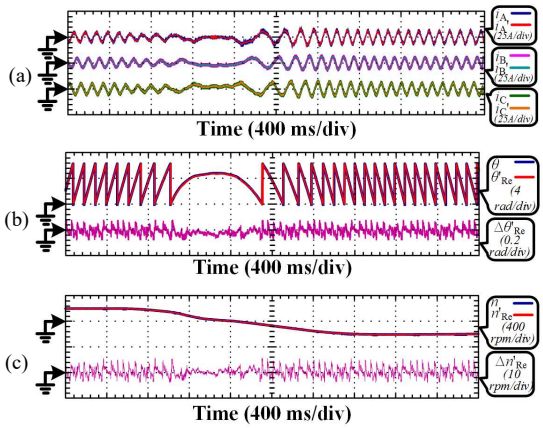

Fig. 13. Experimental results of actual and reconstructed three-phase currents and position estimation in reversing process: (a) Current reconstruction results, (b) Position estimation results, (c) Rotor speed.

The system performance in the speed reversing process are illustrated in Fig.13. Experimental results of current reconstruction, position estimation, and rotor speed estimation are similar with the situations in the starting mode, and good performances are achieved in both of the operational modes.

In Fig.14, the system performance at 750 rpm with the torque of 15 N·m is provided. With the proposed sensorless control by employing the new current phase reconstruction method, the system still shows acceptable performances.

In Fig.15, the system performances in load fluctuation condition is presented. The system performance is not significantly affected by the load fluctuations. Although the position estimation error shows some fluctuations, the error are still controlled within ±0.3 rad.

In order to demonstrate the robustness of over current fault detection in the proposed method. The simulation results of a short-time over current fault is presented in Fig.16. The motor operates at a fast speed reverse condition. Over current is defined as 1.15 times of the rated current, where the instantaneous current reaches 14 A. In the figure, the red dotted lines represent over current values, and a short-time over current fault occurs in phase-A current. It can be seen that, although the over current fault appears very shortly, the reconstructed phase-A current is still able to detect this fault, compared to the actual one.

VI. Conclusion

An independent phase current reconstruction strategy without using null switching states is proposed for IPMSM sensorless control in this paper. The conventional zero vectors, V_{000} and V_{111}, are replaced by the other six basic vectors. To achieve this scheme, the current reconstruction dead zone is divided into six sectors, and each sector is split into three parts with different vector synthesis and corresponding phase current reconstruction methods. Afterwards, the reconstructed three-phase currents are utilized for position estimation. The effectiveness of the proposed IPMSM sensorless control scheme using one single current sensor is verified by the experimental results on a 5 kW IPMSM motor prototype.

From the results, it can be seen that the reconstructed phase

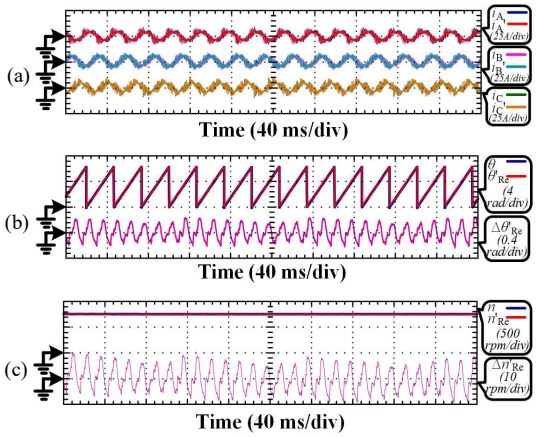

Fig. 14. Experimental results of system performance at 750 rpm and 15 N·m: (a) Current reconstruction results, (b) Position estimation results, (c) Rotor speed.

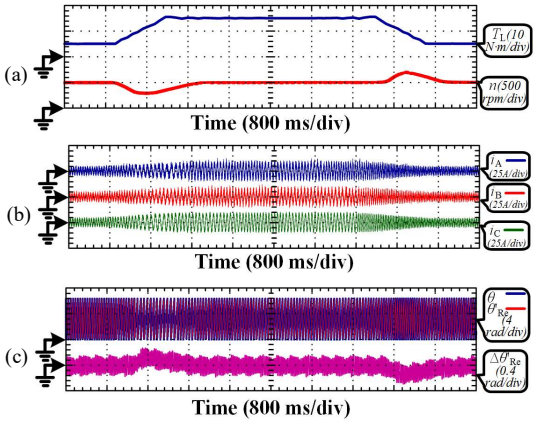

Fig. 15. Experimental results of system performance in load fluctuation conditions: (a) Load and speed, (b) Three phase currents, (c) Position estimation results.

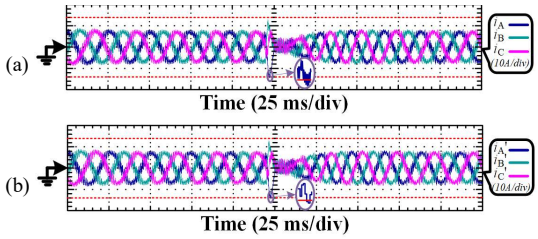

Fig. 16. Simulation results of short-time over current fault with HF signal injection: (a) Actual currents, (b) Reconstructed currents.

currents track the actual currents exactly in different working conditions. Therefore, the estimated rotor position using the actual and reconstructed phase currents are similar with low estimation errors, which are both controlled within about ±0.2 rad. The motor speed follows the command accurately even if the speed or load changes.

1) The phase currents are independently reconstructed in the proposed strategy. Therefore, the reconstructed three-phase currents have higher accuracy compared to those derived by calculating the third phase current according to the values of the other two phase currents.
2) Because the three DC-bus current sampling points are within the period of action vectors, no additional voltage pulses are needed for current reconstruction.
3) The two conventional zero vectors V_{000} and V_{111} are removed from the switching states, hence the zero vectors are synthesized by the rest six available vectors.
4) The proposed vector synthesis method can be utilized both in the current reconstruction dead zones and most of the normal areas. In those normal areas that the proposed method cannot be applied, the circular output range is decreased by $T_{\min}/T_s$.

The proposed scheme can reduce the cost and increase the reliability of IPMSM drive system.

REFERENCES

[1] S. C. Yang, "Saliency-based position estimation of permanent-magnet synchronous machines using square-wave voltage injection with a single current sensor," *IEEE Trans. Ind. Appl.,* vol. 51, no. 2, pp. 1561-1571, Mar./Apr. 2015.

[2] A. Gaeta, G. Scelba, and A. Consoli, "Sensorless vector control of PM synchronous motors during single-phase open-circuit faulted conditions," *IEEE Trans. Ind. Appl.,* vol. 48, no. 6, pp. 1968-1979, *Nov./Dec.* 2012.

[3] Z. Wang, X. Q. Wang, J. W. Cao, M. Cheng, and Y. H. Hu, " Direct torque control of T-NPC inverters fed double-stator-winding PMSM drives with SVM," *IEEE Trans. Power Electron.,* DOI:10.1109/TPEL.2017.2689008, in press, 2017.

[4] S. Medjmadj, D. Diallo, M. Mostefai, C. Delpha, and A. Arias, "PMSM drive position estimation: contribution to the high-frequency injection voltage selection issue," *IEEE Trans. Energy Convers.,* vol. 30, no. 1, pp. 349-358, Mar. 2015.

[5] M. L. Gu, S. Ogasawara, and M. Takemoto, "Novel PWM schemes with multi SVPWM of Sensorless IPMSM drives for reducing current ripple," *IEEE Trans. Power Electron.,* vol. 31, no. 9, pp. 6461-6475, Sep. 2016.

[6] P. L. Xu and Z. Q. Zhu, "Novel square-wave signal injection method using zero-sequence voltage for sensorless control of PMSM drives," *IEEE Trans. Ind. Electron.,* vol. 63, no. 12, pp. 7444-7454, Dec. 2016.

[7] P. L. Xu and Z. Q. Zhu, "Carrier signal injection-based sensorless control for permanent-magnet synchronous machine drives considering machine parameter asymmetry," *IEEE Trans. Ind. Electron.,* vol. 63, no. 5, pp. 2813-2824, May 2016.

[8] Y. Li, Z. Q. Zhu, D. Howe, C. M. Bingham, and D. A. Stone, "Improved rotor-position estimation by signal injection in brushless AC motors, accounting for cross-coupling magnetic saturation," *IEEE Trans. Ind. Appl.,* vol. 45, no. 5, pp. 1843-1850, Sep./Oct. 2009.

[9] G. L. Wang, L. Yang, G. Q. Zhang, X. G. Zhang, and D. G. Xu, "Comparative investigation of pseudorandom high-frequency signal injection schemes for sensorless IPMSM drives," *IEEE Trans. Power Electron.,* vol. 32, no. 3, pp. 2123-2132, Mar. 2017.

[10] D. Panda and V. Ramanarayanan, "Reduced acoustic noise variable DC-bus-voltage-based sensorless switched reluctance motor drive for HVAC applications," *IEEE Trans. Ind. Electron.,* vol. 54, no. 4, pp. 2065-2078, Aug. 2007.

[11] C. T. Lin, C. W. Hung, and C. W. Liu, " Position sensorless control for four-switch three-phase brushless DC motor drives," *IEEE Trans. Power Electron.,* vol. 23, no. 1, pp. 438-444, Jan. 2008.

[12] A. H. Niasar, A. Vahedi, and H. Moghbelli, "a novel position sensorless control of a four-switch, brushless DC motor drive without phase shifter," *IEEE Trans. Power Electron.,* vol. 23, no. 6, pp. 3079-3087, Nov. 2008.

[13] Z. Wang, Y. Zheng, Z. X. Zou, and M. Cheng, "Position sensorless control of interleaved CSI fed PMSM drive with extended Kalman filter," *IEEE Trans. Magn.,* vol. 48, no. 11, pp. 3688-3691, Nov. 2012.

[14] Y. Cho, T. LaBella, and J. S. Lai, "A three-phase current reconstruction strategy with online current offset compensation using a single current sensor," *IEEE Trans. Ind. Electron.,* vol. 59, no. 7, pp. 2924-2933, Jul. 2012.

[15] B. Metidji, N. Taib, L. Baghli, T. Rekioua, and S. Bacha, "Phase current reconstruction using a single current sensor of three-phase AC motors fed by SVM-controlled direct matrix converters," *IEEE Trans. Ind. Electron.,* vol. 60, no. 12, pp. 5497-5505, Dec. 2013.

[16] B. Hafez, A. S. A. Khalik, A. M. Massoud, S. Ahmed, and R. D. Lorenz, "Single-sensor-based three-phase permanent-magnet synchronous motor

drive system with luenberger observers for motor line current reconstruction," *IEEE Trans. Ind. Appl.,* vol. 50, no. 4, pp. 2602-2613, Jul./Aug. 2014.
[17] K. Him and T. M. Jahns, "Phase current reconstruction for AC motor drives using a DC link single current sensor and measurement voltage vectors," *IEEE Trans. Power Electron.,* vol. 21, no. 5, pp. 1413-1419, Sep. 2006.
[18] J. I. Ha, "Current prediction in vector-controlled PWM inverters using single DC-link current sensor," *IEEE Trans. Ind. Electron.,* vol. 57, no. 2, pp. 716-726, Feb. 2010.
[19] K. Sun, Q. Wei, L. P. Huang, and K. Matsuse, "An overmodulation method for PWM-inverter-fed IPMSM drive with single current sensor," *IEEE Trans. Ind. Electron.,* vol. 57, no. 10, pp. 3395-3404, Oct. 2010.
[20] W. Jiang and B. Fahimi, "Current reconstruction techniques for survivable three-phase PWM converters," *IEEE Trans. Power Electron.,* vol. 25, no. 1, pp. 188-192, Jan. 2010.
[21] Y. K. Gu, F. L. Ni, D. P. Yang, and H. Liu, "Switching-state phase shift method for three-phase-current reconstruction with a single DC-link current sensor," *IEEE Trans. Ind. Electron.,* vol. 58, no. 11, pp. 5186-5194, Nov. 2011.
[22] H. Z. Ye and A. Emadi, "A six-phase current reconstruction scheme for dual traction inverters in hybrid electric vehicles with a single DC-link current sensor," *IEEE Transactions on Veh. Technol.,* vol. 63, no. 7, pp. 3085-3093, Sep. 2014.
[23] X. Li, S. Dusmez, B. Akin, and K. Rajashekara, "A new SVPWM for the phase current reconstruction of three-phase three-level T-type converters," *IEEE Trans. Power Electron.,* vol. 31, no. 3, pp. 2627-2637, Mar. 2016.
[24] Y. X. Xu, H. Yan, J. B. Zou, B. C. Wang, and Y. H. Li, "Zero voltage vector sampling method for PMSM three-phase current reconstruction using single current sensor," *IEEE Trans. Power Electron.,* vol. 32, no. 5, pp. 3797-3807, May, 2017.
[25] Y. S. Lai, Y. K. Lin, and C. W. Chen, "New hybrid pulsewidth modulation technique to reduce current distortion and extend current reconstruction range for a three-phase inverter using only DC-link sensor," *IEEE Trans. Power Electron.,* vol. 28, no. 3, pp. 1331-1337, Mar. 2013.
[26] C. L. Xia, Z. Q. Li, and T. N. Shi, "A control strategy for four-switch three-phase brushless DC motor using single current sensor," *IEEE Trans. Ind. Electron.,* vol. 56, no. 6, pp. 2058-2066, Jun. 2009.
[27] W. C. Lee, D. S. Hyun, and T. K. Lee, "A novel control method for three-phase PWM rectifiers using a single current sensor," *IEEE Trans. Power Electron.,* vol. 15, no. 5, pp. 861-870, Sep. 2000.
[28] H. Shin and J. I. Ha, "Phase current reconstructions from DC-link currents in three-phase three-level PWM inverters," *IEEE Trans. Power Electron.,* vol. 29, no. 2, pp. 582-593, Feb. 2014.
[29] Y. Cho, A. Koran, H. Miwa, B. York, and J. S. Lai, "An active current reconstruction and balancing strategy with DC-link current sensing for a multi-phase coupled-inductor converter," *IEEE Trans. Power Electron.,* vol. 27, no. 4, pp. 1697-1705, Apr. 2012.
[30] J. I. Ha, "Voltage injection method for three-phase current reconstruction in PWM inverters using a single sensor," *IEEE Trans. Power Electron.,* vol. 24, no. 3, pp. 767-775, Mar. 2009.
[31] D. P. Marčetić and E. M. Adžić, "Improved three-phase current reconstruction for induction motor drives with DC-link shunt," *IEEE Trans. Ind. Electron.,* vol. 57, no. 7, pp. 2454-2462, Jul. 2010.
[32] H. F. Lu, X. M. Cheng, W. L. Qu, S. Sheng, Y. T. Li, and Z. Y. Wang, "A three-phase current reconstruction technique using single DC current sensor based on TSPWM," *IEEE Trans. Power Electron.,* vol. 29, no. 3, pp. 1542-1550, Mar. 2014.

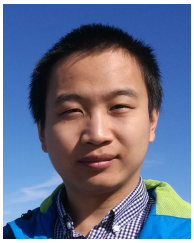

Jiadong Lu was born in Pucheng, China, 1990. He received the B.S. and the M.S. degrees in electrical engineering from Northwestern Polytechnical University, Xi'an, China in 2012 and 2015, respectively, where he is currently working toward the Ph.D. degree.

His research interests include sensorless control and hybrid fault tolerant control techniques for permanent magnet synchronous motor drives.

Xiaokang Zhang was born in Zhejiang, China, in 1992. He received the B.S degree in electrical engineering from Northeast Agricultural University, Harbin, China, in 2015 and he is currently working toward the M.S degree in electrical engineering in Northwestern Polytechnical University. His research interests include sensorless control for permanent magnet synchronous motor and fault tolerant control techniques for motor drives.

Yihua Hu (M'13-SM'15) received the B.S. degree in electrical motor drives in 2003, and the Ph.D. degree in power electronics and drives in 2011, both from China University of Mining and Technology, Jiangsu, China. Between 2011 and 2013, he was with the College of Electrical Engineering, Zhejiang University as a Postdoctoral Fellow. Between November 2012 and February 2013, he was an academic visiting scholar with the School of Electrical and Electronic Engineering, Newcastle University, Newcastle upon Tyne, UK. Between 2013 and 2015, he worked as a Research Associate at the power electronics and motor drive group, the University of Strathclyde. Currently, he is a Lecturer at the Department of Electrical Engineering and Electronics, University of Liverpool (UoL). He has published more than 50 peer reviewed technical papers in leading journals. His research interests include PV generation system, power electronics converters & control, and electrical motor drives.

Jinglin Liu (M'01) received the B.Eng. degree in electrical engineering from Tsinghua University, Beijing, China, in 1986, and the M.Eng. and the Ph.D. degrees in electrical engineering from Northwestern Polytechnical University, Xi'an, China, in 1990 and 2002, respectively. Since 1994, he has been a Faculty Member with Northwestern Polytechnical University, Xi'an, where he is currently a Professor of Electrical Engineering.

His research interests include electrical machines design and drives, power electronics, fault diagnosis, and motion control.

Chun Gan (S'14–M'16) received the B.S. and M.S. degrees in power electronics and motor drives from China University of Mining and Technology, Jiangsu, China, in 2009 and 2012, respectively, and the Ph.D. degree in power electronics and motor drives from Zhejiang University, Hangzhou, China, in 2016.

He is currently a Research Associate with the Department of Electrical Engineering and Computer Science, The University of Tennessee, Knoxville, TN, USA. He is also a member of the U.S. Energy/National Science Foundation cofunded Engineering Research Center CURENT. His research interests include high-efficiency power converters, electric vehicles, electrical motor drives, electrical motor design, continuous variable series reactors, high-voltage direct current transmission, and microgrids.

Zheng Wang (S'05–M'09-SM'14) received the B.Eng. and M.Eng. degrees from Southeast University, Nanjing, China, in 2000 and 2003, respectively, and the Ph.D. degree from The University of Hong Kong, Hong Kong, in 2008, all in electrical engineering.

From 2008 to 2009, he was a Postdoctoral Fellow in Ryerson University, Toronto, ON, Canada. He is currently a full Professor in the School of Electrical Engineering, Southeast University, China. His research interests include electric drives, power electronics, and distributed generation.